

Local pump depletion based angular momentum gain of plasma electrons

Camilla Willim¹†, Thales Silva¹ Luís O. Silva¹ and Jorge Vieira¹

GoLP/Instituto de Plasmas e Fusão Nuclear, Instituto Superior Técnico, Universidade de Lisboa, 1049-001 Lisbon, Portugal

(Received xx; revised xx; accepted xx)

We present a novel mechanism in which plasma electrons optically acquire angular momentum through local pump depletion. This process is facilitated by an azimuthally polarized laser that lacks angular momentum, yet enables electron rotation through canonical momentum conservation. Through theoretical considerations and one- and three-dimensional particle-in-cell simulations, we demonstrate that the electrons acquire substantial angular momentum when the ultra-intense ($I \gtrsim 10^{19}$ W/cm²) and ultra-short (tens of femtoseconds) laser pulse excites a nonlinear wakefield in the bubble regime. During this process, the frequency at the laser's leading edge shifts down due to phase modulation. Following the conservation of the wave action, the laser's vector potential develops a long-wavelength offset that trails the main pulse and remains confined within the plasma bubble. This offset facilitates electron rotation of the bubble's sheath currents and the high-energy (> 100 MeV) self-injected electrons. As the laser pulse front erodes, the long-wavelength offset of the vector potential increases and oscillates, influencing both the magnitude and polarity of the electrons' angular momentum. By varying key laser parameters such as phase, frequency, and polarization, we show how to manipulate and control the transverse momentum space of high-energy electrons.

1. Introduction

The transfer of optical angular momentum plays a critical role in diverse research areas, ranging from the precise control of nano-particle motion (Porfirev *et al.* 2023) to the generation of substantial axial magnetic fields (Talin *et al.* 1975; Najmudin *et al.* 2001; Shi *et al.* 2018), the development of compact accelerators for twisted electron beams with relativistic energies (Vieira *et al.* 2018), and the emission of radiation with angular momentum from the spiral motion of high-energy electrons (Katoh *et al.* 2017; Seipt *et al.* 2014; Luís Martins *et al.* 2019).

Optical angular momentum transfer in underdense plasmas has been studied in the context of the inverse Faraday effect, which was initially explored using circularly polarized lasers (Talin *et al.* 1975; Sheng & Meyer-ter Vehn 1996; Gorbunov & Ramazashvili 1998; Frolov 2004; Naseri *et al.* 2010; Liu *et al.* 2023; Haines 2001; Kostyukov *et al.* 2001; Najmudin *et al.* 2001). Later studies included lasers with orbital angular momentum (Ali *et al.* 2010; Nuter *et al.* 2020; Longman & Fedosejevs 2021), relying on the direct absorption of laser angular momentum. Moreover, angular momentum transfer to plasma waves and energetic charged particles has been demonstrated using laser configurations with orbital angular momentum, such as spatio-temporally coupled beams forming light springs (Vieira *et al.* 2018) and twisted beat waves (Saberri *et al.* 2017; Shi *et al.* 2018).

So far, optically induced plasma electron rotation has primarily been associated with

† Email address for correspondence: camilla.willim@tecnico.ulisboa.pt

circularly polarized lasers and lasers with orbital angular momentum (Allen *et al.* 1992). These lasers exhibit distinct types of angular momentum—spin and orbital—which enable the angular motion of electrons through direct absorption or higher-order nonlinearities (Haines 2001; Sheng & Meyer-ter Vehn 1996; Frolov 2004). The time-averaged angular momentum density of an electromagnetic wave is given by $\vec{M} = \vec{r} \times \langle \vec{E} \times \vec{B} \rangle$, where \vec{E} and \vec{B} are the electric and magnetic field vectors. A laser beam carries angular momentum when the Poynting vector $\langle \vec{E} \times \vec{B} \rangle$ has an azimuthal component.

Here, we demonstrate that electrons can gain angular momentum from lasers without angular momentum, such as azimuthally polarized lasers. Azimuthally polarized laser pulses consist of two orthogonally polarized transverse electromagnetic (TEM₀₁) modes, i.e., TEM_{01(x)} \hat{e}_y – TEM_{01(y)} \hat{e}_x (Oron *et al.* 2000; Nesterov & Niziev 2000). At focus, the vector potential is described by $\vec{A}(r) = a_0(r/w_0) \exp(-r^2/w_0^2) \hat{e}_\theta$, where w_0 is the beam waist and $\hat{e}_\theta = -\sin\theta\hat{e}_x + \cos\theta\hat{e}_y$ is the unit vector in polar direction with $\theta = \tan^{-1}(y/x)$. This configuration exhibits a hollow intensity profile and corresponds to a transverse electric (TE) mode, featuring an electric field component, E_θ , oriented in polar direction and perpendicular to the propagation direction, with radial B_r and axial B_z components of the magnetic field. As a result, its time-averaged Poynting vector is directed along the axis, $\langle \vec{E} \times \vec{B} \rangle = \langle E_\theta B_r \rangle \hat{e}_z$, similar to radial polarization and linearly polarized Gaussian beams (Volke-Sepulveda *et al.* 2002). Therefore, these lasers have zero angular momentum density and thus have not been previously associated with optically induced electron rotation.

In this study, we demonstrate that electrons in a nonlinear wakefield in the blowout regime can acquire substantial angular momentum from azimuthally polarized lasers. Through analytical considerations and one- and three-dimensional particle-in-cell (PIC) simulations using OSIRIS (Fonseca *et al.* 2002), we show that this process arises from canonical momentum conservation and is facilitated by a non-vanishing vector potential that trails the main laser pulse, a phenomenon that develops during local pump depletion (Decker *et al.* 1996; Tsung *et al.* 2002).

In the following, we normalize the electric \vec{E} and magnetic fields \vec{B} to $m_e c \omega_p / e$. The vector potential A is normalized to $m_e c / e$, where the dimensionless vector potential is given by $a_0 = eA / m_e c$. Distances \vec{x} , velocity v , and time t are normalized to c / ω_p , c , and $1 / \omega_p$, respectively. The plasma frequency is defined as $\omega_p = \sqrt{4\pi n_e e^2 / m_e}$, where n_e is the background plasma density and m_e is the electron mass.

2. One-dimensional analysis of local pump depletion and transverse momentum gain of electrons

It is instructive to review the self-consistent laser-plasma dynamics in one dimension to study how the mechanism works. We simulate an ultra-intense short laser pulse with a dimensionless amplitude $a_0 = 6$ ($I \approx 8 \times 10^{19}$ W/cm²) and FWHM pulse duration $\tau = 3 / \omega_p$ (~ 10 fs). The laser is linearly polarized (in y -direction) with a central frequency $\omega_0 = 8 \omega_p$. Initially, the laser pulse's vector potential \vec{A} vanishes (nearly zero) outside the laser pulse. The underdense plasma starts at $z = 34 c / \omega_p$ and is homogeneous with a density of $n_e = 1/64 n_{cr} \approx 2.7 \times 10^{19}$ cm⁻³, where $n_{cr} \approx 1.7 \times 10^{21}$ cm⁻³ corresponds to the critical density for a laser wavelength of $\lambda = 800$ nm. The simulation is performed in a co-moving frame that travels at the speed of light c . The simulation box is $68 c / \omega_p$ long, divided into 6800 cells and one particle per cell.

Figure 1 illustrates how local pump depletion enables the plasma electrons to acquire transverse momentum in a nonlinear wakefield behind the main laser pulse. This process

is driven by a localized frequency downshift at the high-intensity laser pulse front (Fig. 1(a)), the formation of a long-wavelength offset in the laser's vector potential (Fig. 1(b)), which manipulates the electrons transverse momentum through canonical momentum conservation (Fig. 1(c)).

The laser pulse front pushes electrons away from regions of high intensity, thereby modifying the refractive index, $\eta = \sqrt{1 - \omega_p^2/(\omega^2\gamma)}$, through electron density modulation and relativistic mass increase. This interaction ensures that the laser front continuously encounters a positive gradient of the refractive index, $\partial\eta/\partial\xi$, where $\xi = t - z/c$ is the speed of light frame variable. As a result, the laser frequency (and thus the axial wavenumber k_z) shifts down via phase modulation, where the frequency change can be described by $(1/\omega)(\partial\omega/\partial t) \propto -(\partial\eta/\partial\xi)$ (Esarey *et al.* 1990; Mendonça & Silva 1994; Silva & Mendonça 1998; Tsung *et al.* 2002). The plasma frequency ω_p marks the smallest frequency that can propagate. This localized frequency downshift is observable in the Wigner transform of the laser's electric field E_y in Fig. 1(a). The position of the frequency downshift overlaps with the electron density spike (grey line) and the steepened leading edge of the laser pulse's electric field (envelope in red line) (Vieira *et al.* 2010).

The frequency downshift manifests in an increase of the vector potential, which acquires a substantial long-wavelength offset while the electric field appears eroded (Bulanov *et al.* 1992; Decker *et al.* 1996; Tsung *et al.* 2002). This is due to the conservation of the total wave action, $\mathcal{N} \propto |A_y|\omega = \text{constant}$ (Bulanov *et al.* 1992; Tsung *et al.* 2002); the vector potential increases while the laser frequency decreases. As a result, the k_z -spectrum of the vector potential A_y is increased for low wavenumbers, peaking at a few of the plasma wavenumber $k_p = \omega_p/c$ (see Fig. 1(b)).

The longer wavelength components travel with a smaller group velocity, where the group velocity can be approximated by $v_g \simeq c(1 - \omega_p^2/(2\omega^2))$. Thus, in Figure 1(c), we observe a long wavelength offset trailing the main part of the laser pulse. The finite vector potential behind the laser pulse gradually decreases until vanishing at the back of the wakefield. The electrons (blue dots) acquire a finite transverse momentum $p_y = A_y$, following the conservation of canonical momentum (see inset in Fig. 1(c)).

This mechanism has been related to pulse compression (Silva & Mendonça 1998; Tsung *et al.* 2002; Gordon *et al.* 2003; Faure *et al.* 2005) and proposed as a diagnostic for wakefields (Dias *et al.* 1998; Murphy *et al.* 2006; Shiraishi *et al.* 2013; Downer *et al.* 2018). In addition, the concept has been extended to explore the generation of mid-infrared to infrared pulses (Zhu *et al.* 2012, 2013; Chen & Pukhov 2015; Zhu *et al.* 2020; Pai *et al.* 2010; Schreiber *et al.* 2010; Nie *et al.* 2020) and betatron-like radiation from energetic electrons (Lu *et al.* 2021).

In this setup, electrons can be efficiently accelerated due to the high accelerating gradients within the nonlinear wakefield, reaching gradients of GV/m (Esarey *et al.* 1996). Within short propagation distances and times, self-injected electrons become trapped in the wakefield and are accelerated to high energies ($\gtrsim 100$ MeV). In Fig. 2(a), we demonstrate that in addition to their longitudinal acceleration, the high-energy electrons acquire transverse momentum. Specifically, the self-injected electrons with $p_z \gtrsim 140 m_e c$ localized around the same axial position $(z - ct) \approx 16 c/\omega_p$ within the nonlinear wakefield, all contain similar transverse momentum $p_y \approx 0.25 m_e c$ (highlighted in the inset of Fig. 2(a)). This suggests that the electron dynamics are controllable, allowing for manipulation of the beam properties.

Furthermore, during local pump depletion, the transverse momentum of the injected electrons oscillates with increasing magnitude (Nerush & Kostyukov 2009), matching the long wavelength offset of the vector potential, as shown in Fig. 2(b) and (c). The

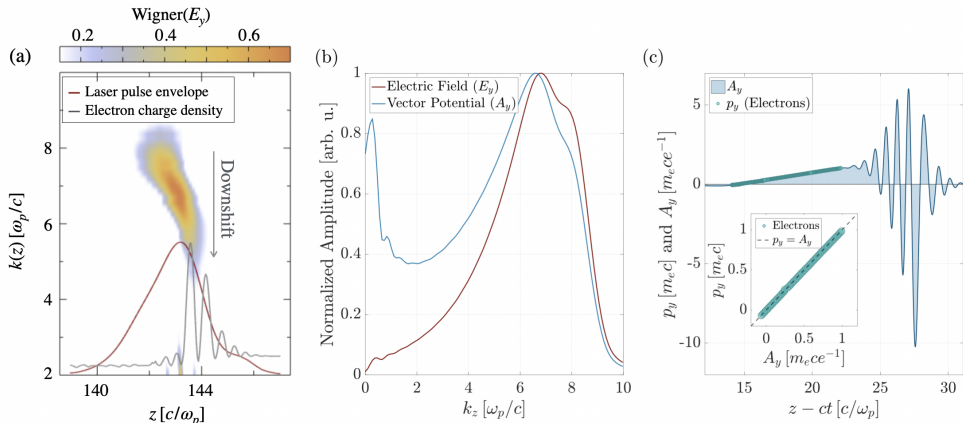


FIGURE 1. One-dimensional OSIRIS simulation results at time $t \approx 116/\omega_p$ showcase the frequency downshift of the laser electric field E_y , which manifests in the vector potential A_y amid local pump depletion, enabling the plasma electrons to acquire transverse momentum in the nonlinear wakefield behind the main laser pulse. (a) The frequency of the laser electric field (envelope of E_y in red) drops at the leading edge (Wigner distribution of E_y) which resides in a steep electron charge density spike (grey line). (b) The normalized amplitude of the low k -spectrum of the vector potential A_y (blue line) surpasses that of the laser's electric field $E_y = -\partial A_y/\partial t$ (red line). (c) The vector potential A_y (blue line) exhibits a long wavelength offset trailing the laser pulse ($(z - ct) \lesssim 25 c/\omega_p$ in the co-moving frame), where the electrons acquire transverse momentum, following canonical momentum conservation $p_y = A_y$ (highlighted in the inset).

oscillation period of the long-wavelength offset of the vector potential is closely linked to the etching velocity—the rate at which the laser's leading edge erodes, defined as $v_{\text{etch}} \approx c(\omega_p^2/\omega_0^2)$ (Decker *et al.* 1996). The oscillation period can be approximated as $T \propto \lambda/v_{\text{etch}}$, where λ is the laser wavelength inside the plasma. In Fig. 2(c), we demonstrate an agreement between the oscillation of the long-wavelength offset and the erosion of the leading edge of the vector potential. The observed period of the oscillation, highlighted by dashed lines indicating $T/2 \approx 25/\omega_p$, matches the theoretical estimate $T/2 \approx (\pi/8) \times 64/\omega_p \approx 25/\omega_p$. This shows that the injection process is influenced by the etching dynamics, making the transverse momentum controllable through the prediction of long-wavelength modulations of the vector potential.

3. Three-dimensional analysis of angular momentum gain of electrons

Building on our one-dimensional analysis, we extend our study to three dimensions, confirming the robustness of electron transverse momentum gain. In this context, we show that plasma electrons acquire angular momentum from a high-intensity azimuthally polarized laser pulse in underdense plasma driving a nonlinear wakefield in the bubble regime (Pukhov & Meyer-ter Vehn 2002). Figure 3 shows the angular momentum of electrons from the bubble's current sheath and injected electrons.

We simulate an azimuthally polarized laser pulse with a dimensionless amplitude of $a_0 = 6$, FWHM pulse duration $\tau = 3/\omega_p$, a central frequency $\omega_0 = 8\omega_p$, and a laser spot size $w_0 = 5.5 c/\omega_p$. Considering a wavelength of $\lambda = 800$ nm, this corresponds to a laser with about 600 mJ, $w_0 = 5.6 \mu\text{m}$, and with pulse duration $\tau \approx 10$ fs propagating in a plasma with density $n_e = 2.7 \times 10^{19}/\text{cm}^3$. The simulation is performed in a co-

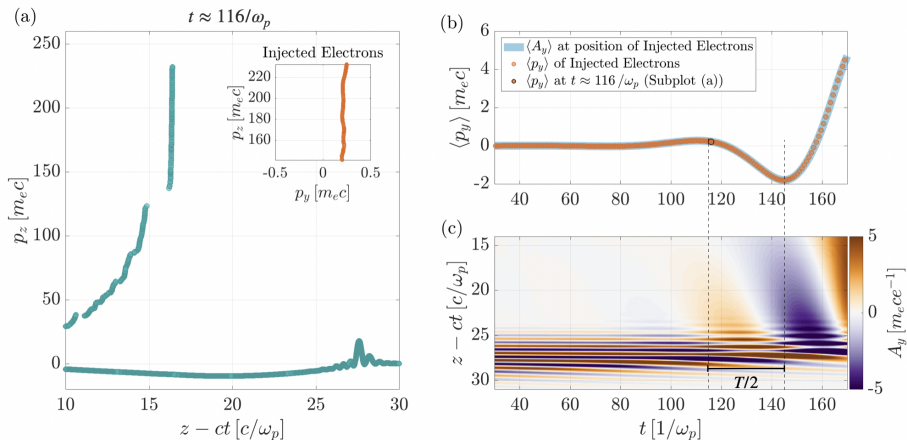


FIGURE 2. One-dimensional OSIRIS simulations show self-injected electron transverse momentum oscillations in a nonlinear wakefield, with increasing magnitude and a period linked to the laser’s leading-edge erosion. (a) The electrons’ position, $z - ct$ in the co-moving frame, and longitudinal momentum, p_z , at time $\approx 116/\omega_p$, show high-energy electrons with $p_z > 140 m_e c$ concentrated at $(z - ct) \approx 16 c/\omega_p$, with their transverse momentum around $p_y \approx 0.25 m_e c$, as highlighted in the inset (orange dots). (b) The time evolution of the mean transverse momentum of the high-energy electrons, $\langle p_y \rangle$, represented by orange dots, aligns well with the corresponding vector potential at their position, $\langle A_y \rangle$, shown as a blue line. The black-circled position corresponds to the time step of subplot (a). (c) The time evolution of the vector potential A_y in the co-moving frame illustrates the erosion of the leading edge and the development of an oscillating long-wavelength offset. The oscillation half-period, $T/2 \approx 25/\omega_p$, is highlighted by dashed lines, illustrating the connection between the erosion of the leading edge, the long-wavelength offset, and the transverse momentum of the electrons shown in (b).

moving frame that travels at the speed of light c . The simulation box has the dimensions $34 \times 34 \times 34(c/\omega_p)^3$, divided into $1700 \times 1700 \times 1700$ cells and 4 particles per cell.

In Fig. 3(a), we present simulation results of an azimuthally polarized laser pulse driving a donut-shaped plasma bubble, reflecting the laser’s hollow intensity distribution (Vieira & Mendonça 2014). The electrons composing the bubble and the self-injected electrons have angular momentum, as indicated by the arrows in blue and orange. Figure 3(b) shows the driver’s vector potential at $t \approx 150/\omega_p$, undergoing local pump depletion and developing a substantial long-wavelength offset that remains confined within the bubble structure. The electrons from the inner and outer current sheaths (highlighted in blue) and the high-energy self-injected electrons (highlighted in orange) possess angular momentum in agreement with canonical momentum conservation, $p_\theta = eA_\theta$ (see inset in Fig. 3(b)). Here, $p_\theta = m_e \gamma r \dot{\theta}$ is the angular momentum, where $\gamma = \sqrt{1 + |\vec{p}|^2}$ is the relativistic factor, $\dot{\theta}$ is the electron’s angular frequency, and A_θ is the laser’s azimuthal vector potential at the position of the electrons (see more on angular momentum conservation in Appendix A). In Fig. 3(c), we highlight the high-energy ($> 200 m_e c^2$) self-injected electrons, forming a ring structure in physical and transverse momentum space. The electrons carry a well-defined angular momentum, with a mean value of $\langle p_\theta \rangle \approx -2 m_e c$. The total charge of these high-energy electrons is $\approx 212 pC$.

Lastly, Fig. 4 demonstrates our simulation results on the manipulation and controllability of angular (transverse) momentum under local pump depletion, focusing on the momentum space evolution of self-injected high-energy electrons. This process is influenced by various parameters, including the initial phase, laser-to-plasma frequency

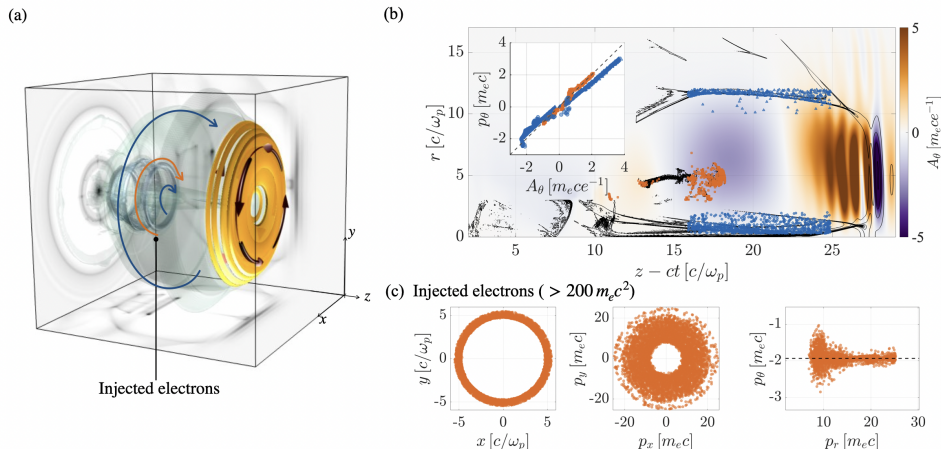


FIGURE 3. Three-dimensional OSIRIS simulation results at $t \approx 150/\omega_p$ illustrate the angular momentum gain of plasma electrons in a nonlinear wakefield, driven by an azimuthally polarized laser pulse – facilitated by the development of a long-wavelength offset in the laser’s azimuthal vector potential due to local pump depletion. (a) The hollow intensity laser pulse (orange isosurfaces) with azimuthal polarization (black arrows) drives a donut-shaped nonlinear wakefield in the bubble regime (gray isosurfaces). Projections show the spatial distribution of the electron charge density, highlighting increased density at the laser pulse front. The blue and orange arrows indicate the direction of rotation of the electrons belonging to the electron sheath composing the donut-shaped bubble (blue) and the injected electrons inside the bubble (orange). The illustrated box dimensions are $20 \times 20 \times 20 (c/\omega_p)^3$. (b) The vector potential A_θ (yellow-purple colormap) exhibits a long-wavelength offset trailing the laser pulse ($z \lesssim 25 c/\omega_p$). Electrons in the inner and outer current sheaths (blue dots) and the self-injected electrons (orange dots) acquire azimuthal momentum following canonical momentum conservation, $p_\theta = A_\theta$, (see inset). (c) The high-energy ($> 200 m_e c^2$) injected electrons form a ring in both physical and transverse momentum space, exhibiting a well-defined angular momentum with a mean value of $\langle p_\theta \rangle \approx -2$ (dashed line).

ratio, laser pulse shape, duration, chirp, and other factors. Here, we examine the effect of three key parameters on the high-energy electrons ($> 80\%$ of the maximum energy) - the initial phase of the laser, which we vary from $\theta_0 = 0$ to 180° (depicted by orange squares in Fig. 4), the laser-to-plasma frequency ratio, which we vary from $\omega_0/\omega_p = 8$ to 6 (depicted by purple diamonds), and the laser polarization where we change from azimuthal to radial polarization (depicted by blue triangles). Radial polarization is composed as $\text{TEM}_{01(x)}\hat{e}_x + \text{TEM}_{01(y)}\hat{e}_y$ (Oron *et al.* 2000; Nesterov & Niziev 2000).

Figure 4(a) shows the evolution of the mean of the electron’s angular momentum $\langle p_\theta \rangle$, exhibiting oscillations with an increasing magnitude. This is influenced by the erosion of the laser pulse front, similar to the one-dimensional case (see Fig. 2(b)). Given the multidimensional structure and transverse focusing fields, the electrons also undergo betatron oscillations with a frequency $\omega_\beta = \omega_p/\sqrt{2\gamma}$ (Tajima & Dawson 1979; Esarey *et al.* 2009), as observed in the radial momentum $\langle p_r \rangle$ in Fig. 4(b). The longitudinal momentum $\langle p_z \rangle$ increases steadily before eventually saturating, as shown in Fig. 4(c). Adjustments to laser parameters influence the polarity, magnitude, and distribution of angular (transverse) momentum of the injected electrons. In Fig. 4(a), we see that varying the laser’s initial phase influences the polarity of the angular momentum $\langle p_\theta \rangle$, but has no influence on the radial and axial momentum. Reducing the laser-to-plasma frequency ratio, impacts the oscillation period and magnitude of the angular momentum, due to the increased etching velocity $v_{\text{etch}} \approx c(\omega_p^2/\omega_0^2)$. It also allows for increased angular

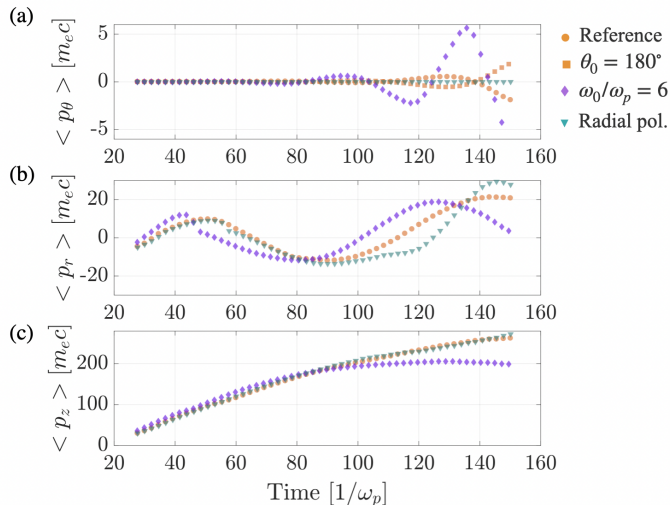


FIGURE 4. Three-dimensional OSIRIS simulation results demonstrate how adjustments of laser parameters allow for the control of angular (transverse) momentum of high-energy electrons ($> 80\%$ of the maximum energy) under local pump depletion. (a) to (c) show the time evolution of the mean azimuthal momentum $\langle p_\theta \rangle$, mean radial momentum $\langle p_r \rangle$, and mean longitudinal momentum $\langle p_z \rangle$, respectively, for different laser and plasma parameters. Orange dots correspond to the reference case with $\theta_0 = 0$, $\omega_0/\omega_p = 8$ and azimuthal polarization; orange squares correspond to a change in the initial laser phase, $\theta_0 = 180^\circ$; purple diamonds represent a change in the laser-to-plasma frequency ratio, $\omega_0/\omega_p = 6$; and blue triangles illustrate the transition to radial polarization. Note that the phase change affects only p_θ , such that the points overlap in (b) and (c).

momentum but the longitudinal momentum saturates more quickly. This can be seen in Fig. 4(c)). On the other hand, radial polarization does not lead to the angular motion but introduces significant modifications to the radial momentum $\langle p_r \rangle$, adding a distinct modulation on top of the betatron oscillations, which becomes prominent as pump depletion progresses ($t > 120/\omega_p$), as shown in Fig. 4(b).

4. Conclusions

In conclusion, we have demonstrated that plasma electrons can acquire substantial angular momentum via canonical momentum conservation, driven by a high-intensity azimuthally polarized laser pulse undergoing local pump depletion in underdense plasma. Through a combination of analytical considerations and particle-in-cell simulations, we explored the mechanism of transverse momentum gain of electrons in one-dimensional scenarios and extended our analysis to three dimensions, obtaining consistent results. This mechanism relied on local pump depletion of the laser pulse, which facilitated the development of a long-wavelength offset in the vector potential trailing the pulse. This offset enabled the rotation of the wakefield's sheath currents and the self-injected electrons. The highest-energy electrons exhibited angular momentum with a small spread and underwent characteristic oscillations linked to the erosion of the laser pulse front. Furthermore, we demonstrated the controllability of angular and transverse momentum gain under local pump depletion by varying key laser parameters, including the initial phase, laser-to-plasma frequency ratio, and polarization.

Future work will aim to test the limits of this scheme, explore exotic laser polarizations, investigate radiation emitted by high-energy electrons, and incorporate ionization effects. Finally, the presented mechanism potentially impacts setups involving lasers with angular momentum such as circularly polarized Gaussian and Laguerre-Gaussian beams, which merits further dedicated investigation.

5. Acknowledgments

We gratefully acknowledge EuroHPC for awarding us access to LUMI-C at CSC (Finland) and Rede Nacional de Computação Avançada (RNCA) for access to Marenumstrum V at the Barcelona Supercomputer Center. This work was supported by the HE EuPRAXIA-PP under grant agreement No. 101079773 and the FCT (Portugal) Foundation for Science and Technology under Project No. X-MASER-2022.02230.PTDC, FCT PD/ BD/142971/2018, UID/FIS/50010/2020, UI/BD/151559/2021, and IPFN-CEEC-INST-LA3/IST-ID.

Appendix A. Angular momentum conservation

The Lagrangian for an electron in an electromagnetic wave in a wakefield can be written as (Jackson 1998)

$$L = -m_e c^2 \left(1 - \frac{\vec{v} \cdot \vec{v}}{c^2} \right)^{1/2} + \frac{e}{c} \vec{v} \cdot \vec{A} - e\phi, \quad (\text{A } 1)$$

where \vec{v} is the velocity vector, c is the speed of light, \vec{A} is the laser's vector potential, ϕ is the scalar potential (here the wakefield potential), and m_e, e are the electron's mass and charge, respectively. Our system is cylindrically symmetric, and for this purpose, we write the Lagrangian in cylindrical coordinates as

$$L = -m_e c^2 \left(1 - \frac{\dot{z}^2}{c^2} - \frac{r^2 \dot{\theta}^2}{c^2} - \frac{\dot{r}^2}{c^2} \right)^{1/2} - e \left(\dot{z} A_z + r \dot{\theta} A_\theta + \dot{r} A_r \right) + e\phi, \quad (\text{A } 2)$$

where $\dot{z} = dz/dt$ is the axial velocity, $\dot{\theta} = d\theta/dt$ is the angular velocity, and $\dot{r} = dr/dt$ is the radial velocity. To determine whether angular momentum is conserved in this system, we calculate the generalized angular momentum

$$P_\theta = \frac{\partial L}{\partial \dot{\theta}} = m_e \gamma r^2 \dot{\theta} - e A_\theta r, \quad (\text{A } 3)$$

where $\gamma = 1/\sqrt{1 - (\dot{z}^2 + r^2 \dot{\theta}^2 + \dot{r}^2)/c^2}$. Here, $m_e \gamma r \dot{\theta} = p_\theta$ is the azimuthal momentum and there is no angular velocity dependence on the wakefield potential, i.e., $\partial\phi/\partial\dot{\theta} = 0$. The generalized angular momentum is conserved when the Hamiltonian, given by

$$H = \sqrt{\left(c\vec{P} - e\vec{A} \right)^2} + m_e^2 c^4 + e\phi, \quad (\text{A } 4)$$

has no angular dependence, i.e.,

$$\frac{dP_\theta}{dt} = -\frac{\partial H}{\partial \theta} = 0. \quad (\text{A } 5)$$

This results in $P_\theta = 0$, because there is no initial angular momentum in the system, such that $p_\theta = eA_\theta$.

This condition holds for a cylindrical vector beam with azimuthal polarization, where

the laser pulse has no angular dependence and the vector potential has only an azimuthal component, $\vec{A} = A_\theta(r, z)\hat{e}_\theta$, where at focus $A(r, 0)_\theta = a_0(r/w_0) \exp(-r^2/w_0^2)$. In this case, plasma electrons can only acquire angular momentum through canonical momentum conservation, $p_\theta = eA_\theta$.

REFERENCES

- ALI, S., DAVIES, J. R. & MENDONÇA, J. T. 2010 Inverse Faraday Effect with Linearly Polarized Laser Pulses. *Phys. Rev. Lett.* **105** (3), 035001.
- ALLEN, L., BEIJERSBERGEN, M. W., SPREEUW, R. J. C. & WOERDMAN, J. P. 1992 Orbital angular momentum of light and the transformation of laguerre-gaussian laser modes. *Phys. Rev. A* **45** (11), 8185.
- BULANOV, S. V., INOVENKOV, I. N., KIRSANOV, V. I., NAUMOVA, N. M. & SAKHAROV, A. S. 1992 Nonlinear depletion of ultrashort and relativistically strong laser pulses in an underdense plasma. *Phys. Fluids B* **4** (7), 1935–1942.
- CHEN, Z. Y. & PUKHOV, A. 2015 High field terahertz emission from relativistic laser-driven plasma wakefields. *Phys. Plasmas* **22** (10), 103105.
- DECKER, C. D., MORI, W. B., TZENG, K.-C. & KATSIOULEAS, T. 1996 The evolution of ultra-intense, short-pulse lasers in underdense plasmas. *Phys. Plasmas* **3** (5), 2047–2056.
- DIAS, J. M., SILVA, L. O. & MENDONÇA, J. T. 1998 Photon acceleration versus frequency-domain interferometry for laser wakefield diagnostics. *Physical Review Special Topics-Accelerators and Beams* **1** (3), 031301.
- DOWNER, M. C., ZGADZAJ, R., DEBUS, A., SCHRAMM, U. & KALUZA, M. C. 2018 Diagnostics for plasma-based electron accelerators. *Rev. Mod. Phys.* **90** (3), 035002.
- ESAREY, E., SCHROEDER, C. B. & LEEMANS, W. P. 2009 Physics of laser-driven plasma-based electron accelerators. *Rev. Mod. Phys.* **81** (3), 1229–1285.
- ESAREY, E., SPRANGLE, P., KRALL, J. & TING, A. 1996 Overview of plasma-based accelerator concepts. *IEEE Trans. Plasma Sci.* **24** (2), 252–288.
- ESAREY, E., TING, A. & SPRANGLE, P. 1990 Frequency shifts induced in laser pulses by plasma waves. *Phys. Rev. A* **42** (6), 3526.
- FAURE, J., GLINEC, Y., SANTOS, J. J., EWALD, F., ROUSSEAU, J.-P., KISELEV, S., PUKHOV, A., HOSOKAI, T. & MALKA, V. 2005 Observation of laser-pulse shortening in nonlinear plasma waves. *Phys. Rev. Lett.* **95** (20), 205003.
- FONSECA, R. A., SILVA, L. O., TSUNG, F. S., DECYK, V. K., LU, W., REN, C., MORI, W. B., DENG, S., LEE, S., KATSIOULEAS, T. & OTHERS 2002 Osiris: A three-dimensional, fully relativistic particle in cell code for modeling plasma based accelerators. In *Computational Science—ICCS 2002: International Conference Amsterdam, The Netherlands, April 21–24, 2002 Proceedings, Part III 2*, pp. 342–351. Springer.
- FROLOV, A. A. 2004 Excitation of magnetic fields by a circularly polarized laser pulse in a plasma channel. *Plasma Phys. Rep.* **30** (8), 698–709.
- GORBUNOV, L. M. & RAMAZASHVILI, R. R. 1998 Magnetic field generated in a plasma by a short, circularly polarized laser pulse. *J. Exp. Theor. Phys.* **87** (3), 461–467.
- GORDON, D. F., HAFIZI, B., HUBBARD, R. F., PENANO, J. R., SPRANGLE, P. & TING, A. 2003 Asymmetric self-phase modulation and compression of short laser pulses in plasma channels. *Phys. Rev. Lett.* **90** (21), 215001.
- HAINES, M. G. 2001 Generation of an Axial Magnetic Field from Photon Spin. *Phys. Rev. Lett.* **87** (13), 135005.
- JACKSON, J. D. 1998 *Classical Electrodynamics*, 3rd edn. Wiley.
- KATOH, M., FUJIMOTO, M., KAWAGUCHI, H., TSUCHIYA, K., OHMI, K., KANEYASU, T., TAIRA, Y., HOSAKA, M., MOCHIHASHI, A. & TAKASHIMA, Y. 2017 Angular momentum of twisted radiation from an electron in spiral motion. *Phys. Rev. Lett.* **118** (9), 094801.
- KOSTYUKOV, I., SHVETS, G., FISCH, N. J. & RAX, J. M. 2001 Inverse Faraday effect in a relativistic laser channel. *Laser Part. Beams* **19** (1), 133–136.
- LIU, W., JIA, Q. & ZHENG, J. 2023 Inverse faraday effect of weakly relativistic full poincaré beams in plasma. *Matter Radiat. Extrem.* **8** (1).

- LONGMAN, A. & FEDOSEJEVS, R. 2021 Kilo-Tesla axial magnetic field generation with high intensity spin and orbital angular momentum beams. *Phys. Rev. Research* **3** (4), 043180.
- LU, Y., ZHANG, G., ZHAO, J., HU, Y., ZHANG, H., LI, D., LI, Q., CAO, Y., WU, Y., YIN, Y. & OTHERS 2021 Ultra-brilliant gev betatronlike radiation from energetic electrons oscillating in frequency-downshifted laser pulses. *Opt. Express* **29** (6), 8926–8940.
- LUÍS MARTINS, J., VIEIRA, J., FERRI, J. & FÜLÖP, T. 2019 Radiation emission in laser-wakefields driven by structured laser pulses with orbital angular momentum. *Sci. Rep.* **9** (1), 9840.
- MENDONÇA, J. T. & SILVA, L. O. 1994 Regular and stochastic acceleration of photons. *Physical Review E* **49** (4), 3520.
- MURPHY, C. D., TRINES, R. M. G. M., VIEIRA, J., REITSMA, A., BINGHAM, R., COLLIER, J. L., DIVALL, E. J., FOSTER, P. S., HOOKER, C. J., LANGLEY, A. J. & OTHERS 2006 Evidence of photon acceleration by laser wake fields. *Phys. Plasmas* **13** (3).
- NAJMUDIN, Z., TATARAKIS, M., PUKHOV, A., CLARK, E. L., CLARKE, R. J., DANGOR, A. E., FAURE, J., MALKA, V., NEELY, D., SANTALA, M. I. K. & KRUSHELNICK, K. 2001 Measurements of the Inverse Faraday Effect from Relativistic Laser Interactions with an Underdense Plasma. *Phys. Rev. Lett.* **87** (21), 215004.
- NASERI, N., BYCHENKOV, V. YU. & ROZMUS, W. 2010 Axial magnetic field generation by intense circularly polarized laser pulses in underdense plasmas. *Phys. Plasmas* **17** (8), 083109.
- NERUSH, E. N. & KOSTYUKOV, I. Y. 2009 Carrier-envelope phase effects in plasma-based electron acceleration with few-cycle laser pulses. *Physical Review Letters* **103** (3), 035001.
- NESTEROV, A. V. & NIZIEV, V. G. 2000 Laser beams with axially symmetric polarization. *J. Phys. D: Appl. Phys.* **33** (15), 1817–1822.
- NIE, Z., PAI, C.-H., ZHANG, J., NING, X., HUA, J., HE, Y., WU, Y., SU, Q., LIU, S., MA, Y. & OTHERS 2020 Photon deceleration in plasma wakes generates single-cycle relativistic tunable infrared pulses. *Nat. Commun.* **11** (1), 2787.
- NUTER, R., KORNEEV, PH., DMITRIEV, E., THIELE, I. & TIKHONCHUK, V. T. 2020 Gain of electron orbital angular momentum in a direct laser acceleration process. *Phys. Rev. E* **101** (5), 053202.
- ORON, R., BLIT, S., DAVIDSON, N., FRIESEM, A. A., BOMZON, Z. & HASMAN, E. 2000 The formation of laser beams with pure azimuthal or radial polarization. *Appl. Phys. Lett.* **77** (21), 3322–3324.
- PAI, C., CHANG, Y., HA, L., XIE, Z., LIN, M., LIN, J., CHEN, Y., TSAUR, G., CHU, H., CHEN, S. & OTHERS 2010 Generation of intense ultrashort midinfrared pulses by laser-plasma interaction in the bubble regime. *Phys. Rev. A* **82** (6), 063804.
- PORFIREV, A., KHONINA, S. & KUCHMIZHAK, A. 2023 Light–matter interaction empowered by orbital angular momentum: Control of matter at the micro-and nanoscale. *Prog. Quantum Electron.* **88**, 100459.
- PUKHOV, A. & MEYER-TER VEHN, J. 2002 Laser wake field acceleration: the highly non-linear broken-wave regime. *Appl. Phys. B* **74**, 355–361.
- SABERI, H., VIEIRA, J. & SILVA, L. O. 2017 Ponderomotive beatwave ion acceleration using twisted light. *Phys. Plasmas* **24** (10).
- SCHREIBER, J., BELLEI, C., MANGLES, S. P. D., KAMPERIDIS, C., KNEIP, S., NAGEL, S. R., PALMER, C. A. J., RAJEEV, P. P., STREETER, M. J. V. & NAJMUDIN, Z. 2010 Complete temporal characterization of asymmetric pulse compression in a laser wakefield. *Phys. Rev. Lett.* **105** (23), 235003.
- SEIPT, D., SURZHYKOV, A. & FRITZSCHE, S. 2014 Structured x-ray beams from twisted electrons by inverse compton scattering of laser light. *Phys. Rev. A* **90** (1), 012118.
- SHENG, Z. M. & MEYER-TER VEHN, J. 1996 Inverse Faraday effect and propagation of circularly polarized intense laser beams in plasmas. *Phys. Rev. E* **54** (2), 1833–1842.
- SHI, Y., VIEIRA, J., TRINES, R. M. G. M., BINGHAM, R., SHEN, B. F. & KINGHAM, R. J. 2018 Magnetic Field Generation in Plasma Waves Driven by Copropagating Intense Twisted Lasers. *Phys. Rev. Lett.* **121** (14), 145002.
- SHIRAIISHI, S., BENEDETTI, C., GONSALVES, A. J., NAKAMURA, K., SHAW, B. H., SOKOLLIK, T., VAN TILBORG, J., GEDDES, C. G. R., SCHROEDER, C. B., TÓTH, C. & OTHERS

- 2013 Laser red shifting based characterization of wakefield excitation in a laser-plasma accelerator. *Phys. Plasmas* **20** (6).
- SILVA, L. O. & MENDONÇA, J. T. 1998 Kinetic theory of photon acceleration: Time-dependent spectral evolution of ultrashort laser pulses. *Phys. Rev. E* **57** (3), 3423.
- TAJIMA, T. & DAWSON, J. M. 1979 Laser electron accelerator. *Phys. Rev. Lett.* **43** (4), 267.
- TALIN, B., KAFTANDJIAN, V. P. & KLEIN, L. 1975 Inverse Faraday effect in plasmas. *Phys. Rev. A* **11** (2), 648–657.
- TSUNG, F. S., REN, C., SILVA, L. O., MORI, W. B. & KATSIOULEAS, T. 2002 Generation of ultra-intense single-cycle laser pulses by using photon deceleration. *Proc. Natl. Acad. Sci. U.S.A.* **99** (1), 29–32.
- VIEIRA, J., FIÚZA, F., SILVA, L. O., TZOUFRAS, M. & MORI, W. B. 2010 Onset of self-steepening of intense laser pulses in plasmas. *New J. Phys.* **12** (4), 045025.
- VIEIRA, J. & MENDONÇA, J.T. 2014 Nonlinear Laser Driven Donut Wakefields for Positron and Electron Acceleration. *Phys. Rev. Lett.* **112** (21), 215001.
- VIEIRA, J., MENDONÇA, J.T. & QUÉRÉ, F. 2018 Optical Control of the Topology of Laser-Plasma Accelerators. *Phys. Rev. Lett.* **121** (5), 054801.
- VOLKE-SEPULVEDA, K., GARCÉS-CHAVEZ, V., CHAVEZ-CERDA, S., ARLT, J. & DHOLAKIA, K. 2002 Orbital angular momentum of a high-order Bessel light beam. *J. Opt. B: Quantum Semiclass. Opt.* **4**, S82.
- ZHU, W., PALASTRO, J. P. & ANTONSEN, T. M. 2012 Studies of spectral modification and limitations of the modified paraxial equation in laser wakefield simulations. *Phys. Plasmas* **19** (3).
- ZHU, W., PALASTRO, J. P. & ANTONSEN, T. M. 2013 Pulsed mid-infrared radiation from spectral broadening in laser wakefield simulations. *Phys. Plasmas* **20** (7).
- ZHU, X., WENG, S., CHEN, M., SHENG, Z. & ZHANG, J. 2020 Efficient generation of relativistic near-single-cycle mid-infrared pulses in plasmas. *Light: Sci. Appl.* **9** (1), 46.